Materials Chemistry and Physics 294 (2023) 127032

Contents lists available at ScienceDirect

Materials Chemistry and Physics

journal homepage: www.elsevier.com/locate/matchemphys

Enhanced energy-storage density of $BaTi_{0.95}Zr_{0.05}O_3$ via generation of defect dipoles upon lithium-doping

Mahmoud S. Alkathy [a,*], Attaur Rahaman [a], Valmor R. Mastelaro [b], Flavio Paulo Milton [a,c], Fabio L. Zabotto [a], Manuel H. Lente [d], Alexandre Strabello [a], J.A. Eiras [a,**]

[a] Physics Department, Federal University of São Carlos, CEP 13565-905, São Carlos, São Paulo, Brazil
[b] Institute of Physics University of São Paulo, São Carlos, CEP 13566-590, São Carlos, São Paulo, Brazil
[c] Federal University of Grande Dourados Faculty of Exact Sciences and Technology - FACET Applied Optics Group (GOA) Dourados, CEP 79825-070, MS, Brazil
[d] Instituto de Ciência e Tecnologia, Universidade Federal de São Paulo, São José dos Campos, CEP 12231-280, São José dos Campos, SP, Brazil

HIGHLIGHTS

- Successful preparation of $BaTi_{0.95}Zr_{0.05}O_3$ (BZT) based ceramics.
- This study shows how to improve the energy storage properties of perovskite materials.
- Pinched hysteresis loops with high P_{max} and small P_r are observed at high Li-ion content.
- The onset of defect dipoles induced by acceptor ions improve the energy storage density.
- Improving energy storage properties by inducing defect dipoles is a new approach.

GRAPHICAL ABSTRACT

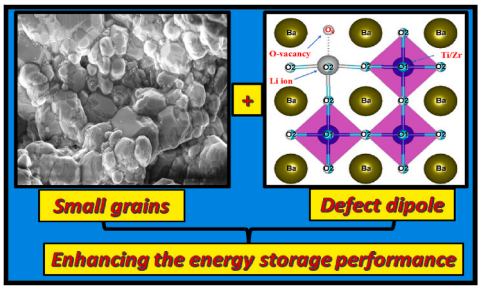

ARTICLE INFO

Keywords:
Acceptor dopants
Oxygen vacancies
Defect dipoles
Remnant polarization
Enegy storag density
Energy storage efficiency

ABSTRACT

Researchers seek the most optimal solutions to a worsening crisis and escalating energy demand. In light of this, ferroelectric (FE) ceramics have become increasingly important. In perovskite oxides, defect dipoles can significantly influence the dynamics of oxygen vacancies. The lithium ions were selected as acceptor ions doped Ba site of $BaTi_{0.95}Zr_{0.05}O_3$ (BZT) based ceramics. A systematic investigation of its effect on the structural, dielectric, ferroelectric, and energy storage properties has been conducted. This study shows how to improve the energy storage density and efficiency by creating defect dipoles on the (BZT) host lattice. The obtained results indicate that Li-doping plays an essential role in changing the shape of hysteresis loops. Pinched hysteresis loops with high maximum polarization and small remnant polarization were acquired when the doping content was raised due to increasing the defect dipoles. Following the onset of defect dipoles induced by acceptor ions, the recoverable energy density increased from 0.191 J/cm^3 to 0.701 J/cm^3. In contrast, the energy storage efficiency increased 12th times compared to pure one, i.e., from 7% to 81%. The BLZT0.08 sample is also exceptionally stable over a range of temperatures and frequencies, making them a good candidate for applications in the field of energy storage. Improving energy storage density and efficiency by inducing defect dipoles in ferroelectric host-lattice may be one of the attractive approaches to developing ferroelectric materials for energy storage applications.

* Corresponding author.
** Corresponding author.
E-mail addresses: alkathy@df.ufscar.br (M.S. Alkathy), eiras@df.ufscar.br (J.A. Eiras).

https://doi.org/10.1016/j.matchemphys.2022.127032
Received 24 June 2022; Received in revised form 9 November 2022; Accepted 11 November 2022
Available online 13 November 2022

1. Introduction

Energy consumption rises as the global population increases, and more connected devices are used, necessitating the development of energy storage systems. We cannot use renewable energies continuously (e. g., wind energy is available primarily in the mornings, and solar in the daytime). Providing electronic devices with readily available electrical energy is a primary solution that converts harvested renewable energy into electrical energy and stores it for any use. We can achieve this by obtaining efficient electrical energy storage tuned to a specific application. There are four main types of energy storage systems, namely 1. Solid oxide fuel cells (SOFCs); 2. Lithium-ion batteries; 3. Electrochemical capacitors; and 4. dielectrics capacitors [1–3]. In general, energy density and power density are the two most important parameters to determine the suitability of any electric energy storage devices for a specific application [4,5]. In this sense, dielectric capacitors can deliver charges quickly, while traditional batteries are less efficient due to their chemical reactions [6–8].

Additionally, dielectric capacitors usually have a longer lifespan for the same reason batteries do not always have complete reversible chemical reactions [9–13]. Based on that, ferroelectric perovskite materials are attractive materials with intense research interest in developing the electronic devices for multifunctional applications [14–17]. For example, with the rapid development of electronic device, advanced materials with high dielectric constant, low loss, and good temperature stability are in great demand for potential applications in advanced energy storage [18–22]. In principle, the materials with high maximum polarization (P_{max}), small remnant polarization (P_r), and higher electrical breakdown strength (E_b) are the best promising materials for enhancing energy storage performance [23–28]. High energy capacity can be achieved using materials with high dielectric permittivity and high breakdown voltage [29–32]. Due to bipolar polarization, high dielectric materials are generally associated with ferroelectric materials and are extensively used in electrostatic capacitors because of their high k properties [33–35]. Based on this criterion, four types of materials, especially antiferroelectric, dielectric glass-ceramic, relaxer ferroelectric, and polymer-based ferroelectric materials, are likely to be used in the subsequent developments of supercapacitors, and they have been extensively studied [36–40]. Recently, several studies have reported that the breakdown strength and dielectric constant can be enhanced in BT by a single or co-doping process [41–44]. In acceptor doping, the valence state of the dopant is smaller than that of doping ions, while in donor doping, the valence state of the dopant is more significant than that of the substituted ions [45–48]. For example, lithium's valence state of dopant is smaller than that of Ba^{2+} and Ti^{4+} ions. As per the literature, the Li^{+} has been possible to occupy the Ba^{2+} site, Ti^{4+} site, and interstitial sites in either an order or disorder manner resulting in the creation of oxygen vacancies on the $BaTiO_3$ matrix [49,50]. The lithium ions also were used as additives to decrease the sintering temperature of $BaTiO_3$ [51–53]. Also, it is interesting to note that the grain size of dielectric ceramics significantly impacts their energy storage performance [54]. According to the grain size effect, ceramic materials with fine grains can achieve high breakdown strength, ultralow Pr, and low coercive electric field [54]. Also, Zr ions doped in the Ti site of $BaTiO_3$ resulted in the thermal stability of the maximum dielectric permittivity over a temperature range [55], an essential requirement in energy storage capacitors.

Furthermore, it is well known that when ceramics are doped with acceptor atoms, oxygen vacancies are introduced by valence compensation [55]. The acceptor atoms and oxygen vacancies then combine to create electric dipoles, also known as complex defects [55–58], which are parallel to the polar direction of the domains in the pure state [59]. Low remnant polarization values result from these defects acting naturally as pinning sites for the domain rotation [60].

Furthermore, complex defects have been demonstrated to diminish the remnant polarization compared to the defect-free situation [61]. However, it is also believed that when an external electric field is switched, ferroelectric domains have the propensity to reorient, pushing defects to realign perpendicular to the polar direction of domains and thereby initiating a depinning process of the switchable domains [55]. These highly intriguing characteristics motivate us to investigate the dynamics of pinching the hysteresis loops in polycrystalline materials in depth, taking into account the impact of this phenomenon on the effectiveness of energy storage performance. In this study, we used hysteresis loop measurements to examine the energy storage performance in Li^{+}-doped BZT ceramics to describe the defect dipoles in ferroelectric bulk ceramics comprehensively and to discover the impact of defects on the performance of energy storage. The results show that incorporating Li^{+} ions on the BZT lattice affects the hysteresis loop caused by the defect dipoles along the spontaneous polarization direction. The defect dipoles remain in the original orientation since defects have a low migration rate, thus restoring the switched polarization and causing a big difference between P_r and P_{max}. The detailed study performed in this work can help open the door for researchers to develop energy storage applications.

2. Experimental

Polycrystalline of $(Ba_{1-x}Li_x)Ti_{0.95}Zr_{0.05}O_3$ ceramics abbreviated as (BLZTx) where ($0 \leq x \leq 0.08$) were synthesized by using the solid-state reaction method. The starting materials used to make this composition were $BaCO_3$, Li_2CO_3, ZrO_2 (Sigma-Aldrich, 99.99% purity), and TiO_2 (Sigma-Aldrich, 99.98% purity). Initially, the materials were weighed, then ball-milled in acetone using zirconia balls for 8 h and calcined at 1100 °C with a dwell time of 6 h using a conventional furnace. Once the powders were calcined, they were ball-milled for another 8 h and sieved to ensure particle homogeneity, Following the addition of 1 wt% Polyvinyl Alcohol (PVA) as a binder, green pellets 10 mm in diameter and 1 mm thick were fabricated. The grain pellets are showily heated (2 °C/min) to 500 °C and kept at this temperature for 1 h to evaporate the binder. Consequently, the green pellets were sintered using a conventional furnace at 1400 °C for 8 h in the air with a heating and cooling rate of 5 °C/min. The X-ray diffraction pattern of all investigated samples was recorded using a Bruker D8 powder XRD at room temperature with a scanning rate of 2°/min over the angular range 2θ of 10°–80°. Rietveld refinement was used to examine the XRD data further using the Fullprof software. The Micro-Raman spectrometer was equipped with a 532 nm s harmonic Nd: YAG laser excitation source. The microstructure study of the sintered samples was carried out using SEM and Transmission electron microscopy (TEM). The grain size was estimated using ImageJ software. X-ray Photoelectron Spectroscopy (XPS) for the BLZT:0.08 sample was carried out using the Scienta Omicron ESCA + spectrometer with monochromatic X-ray source Al-Kα (1486.7 eV, with a power of 280 W and a constant pass energy mode of 50 eV). The sintered samples were polished for electrical measurements, reduced the thickness to 0.45 mm, and fabricated the electrodes using silver paste. The temperature dependence of dielectric permittivity was measured over RT-300 °C at 1 kHz using an impedance analyzer (Agilent E4294A). The ferroelectric study was carried out at room temperature and a frequency of 10 Hz using a homemade setup based on a sawyer-tower circuit. The energy storage properties are theoretically estimated from the integration of the *P-E* hysteresis loop.

3. Results and discussion

Fig. 1(a) exhibits the XRD patterns of BLZT:x ($0\% \leq x \leq 8\%$) ceramics. The observed peaks reveal the single tetragonal phase with no detection of any secondary phase. XRD patterns matched the powder diffraction standards (JCPDS file no #83–1880) of perovskite $BaTiO_3$ ceramics [62]. Rietveld refinement has been applied to validate the lattice constant variation, unit cell volume, bond lengths, and bond angles. The obtained result is exhibited in Fig. 1(b). We used the

pseudo-Voigt function for the peak fitting. The obtained parameters, such as lattice constants, unit cell volume, theoretical density, and R-factors of the investigated samples, are recorded in Table 1. R_p, R_{wp}, R_B, and χ^2 are below 10% in all fitted data, which indicates the lattice constant is believable. The lattice constants (*a*) and (*c*), bond length, and tetragonality (*c/a*) are shown in Fig. 2(a)-(c); it is clear from Fig. 2(a) that the lattice parameter (a = b) decreases with rising Li^+ concentration. Accordingly, reduce the unit cell. The decrease in unit cell volume could be ascribed to the fact that the Li^+-ions Li^+(0.73 Å) with 12-coordination is a smaller ionic radius than Ba^{2+}(1.43 Å) [63], occupied the Ba^{2+}-site. Based on this analysis, it can be assumed that Li^+ enters into the Ba-site of the BZT host-lattice. A similar observation was reported by Lou, Q et al. [64] in Li-doped $BaTiO_3$ ceramics. These phenomena lead tetragonality to decrease when x increases, as shown in Fig. 2(c). The crystal structure of BZT is designed as shown in Fig. 1(b). The crystallite size of the investigated sample in the nano-range from high-resolution TEM in Fig. 1(c). The irregular crystallite shape is observed in the TEM image in Fig. 1(c). The tetragonality of BZT decreases with increased Li^+ concentration and is significantly correlated with decreasing remnant polarization, as discussed in the ferroelectric section. Hence, it is reported that the tetragonal distortion, i.e., c/a ratio, significantly affects the switching behaviours of ferroelectrics [65]. Fig. 2(a–c) shows the variation of unit cell parameters, bond length, and tetragonality with dopant concentration (see Table 1).

In addition to X-ray diffraction, Raman spectroscopy was used to discover eventual low concentrations of impurities not visible in X-ray diffraction, crystal structures in the host material, evaluate the relaxer-like behaviour, and distortions involving ionic radius differences between the dopants [66]. Raman spectra of BLZT:x ceramics detected at wavenumbers range of (200–900) cm^{-1}, measured at room temperature, are shown in Fig. 3. A group theory analysis indicates that there are three fundamental O modes for $BaTiO_3$ (BT) - 260 cm^{-1} for $A_1(TO_2)$, 520 cm^{-1} for $A_1(TO_3)$, and 720 cm^{-1} for $A_1(LO)$ - and a mode at 307 cm^{-1} for $E(TO_3)$ [67]. In addition to the BT similar modes, BZT, BLZT0.02, BLZT:0.04, and BLZT:0.08 present additional methods in the

Table 1
Calculated parameters from Rietveld Refinement of X-ray Diffraction for BLZT:x ($0 \leq x \leq 0.08$) ceramics at room temperature.

Sample	BLZT0	BLZT0.02	BLZT0.04	BLZT0.08
Crystal System	Tetragonal	Tetragonal	Tetragonal	Tetragonal
a = b (Å)	4.0219	4.0187	4.01136	4.00808
c (Å)	4.0379	4.03033	4.0207	4.01019
c/a	1.00398	1.00289	1.00233	1.00053
V $(Å)^3$	65.31578	65.08963	64.69712	64.42252
Space group	*P4mm*	*P4mm*	*P4mm*	*P4mm*
SG No.	99	99	99	99
(Ti/Zr–O1) (Å)	1.9854(4)	1.9817(4)	1.9770(4)	1.9718(4)
(Ti/Zr–O1) (Å)	2.0525(4)	2.0486(4)	2.0437(4)	2.0384(4)
(Ti/Zr–O2) (Å)	2.02093(15)	2.01432(15)	2.01064(15)	2.00898(15)
(O1–Ti/Zr–O1) (°)	180	180	180	180
(O2–Ti/Zr–O2) (°)	171.957 ± 0.016	171.958 ± 0.017	171.948 ± 0.011	169.622 ± 0.011
(O1–Ti/Zr–O1) Tilting angle (°)	4.021 ± 0.0055	4.020 ± 0.0027	4.025 ± 0.0017	5.188 ± 0.0011
Density g/cm^3	5.214	6.125	5.531	5.564
R_p (%)	3.92	8.30	8.19	6.74
R_{wp} (%)	5.95	10.2	11.3	9.94
R_{ex} (%)	4.12	9.53	8.37	9.74
χ^2	2.08	1.15	1.82	1.04

spectra that can be summarized as follows: $E(TO_2)$ mode located at around 199-200 cm^{-1} which is related to the displacement of Li^+ ions in Ba–O vibrations; $A_1(TO_2)$, $E(TO_3)$, and $E(LO_3)$ modes located in the wavenumber range of around 258-350 cm^{-1} related to the displacement of Ti/Zr–O vibrations modes, $A_1(TO_3)$ and $E(LO_4)$ modes related to a mixture of bending and stretching (Ti/ZrO_6) octahedral, $A_1(LO_3)$ mode located at around 720 cm^{-1} associated with octahedral distortion in ferroelectric phase. According to Refs. [68–70], the peak at 300 cm^{-1} is indicative of tetragonal behaviour in BT. The decrease of intensity of this peak indicates a reduction in the tetragonality with an increase in the Li-content, which agrees with XRD results. The incorporation of Li into

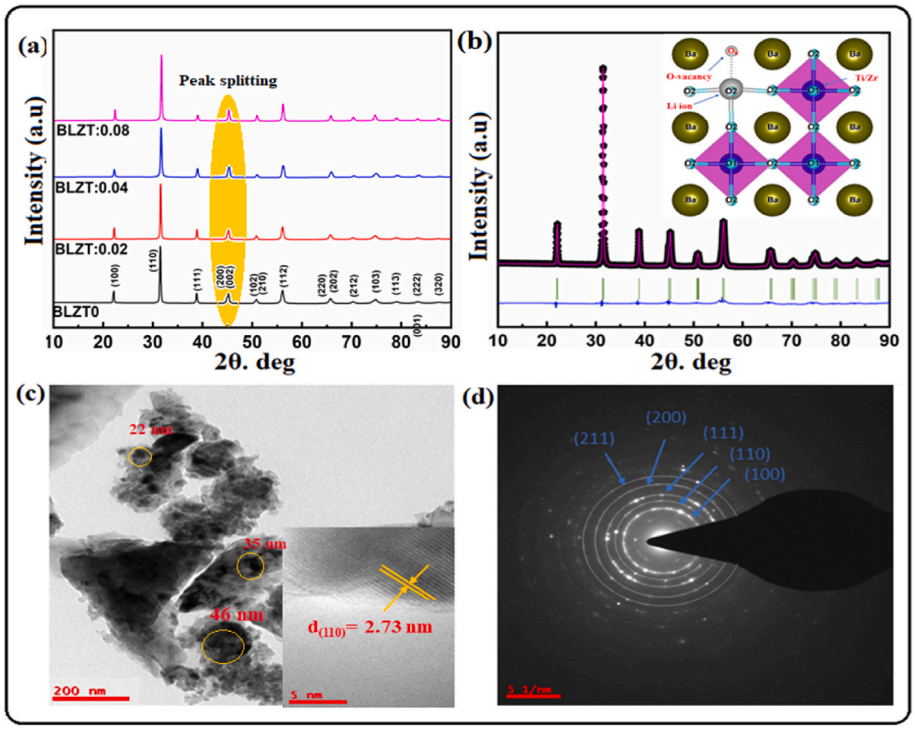

Fig. 1. (a) XRD pattern of BLZT:x ceramics investigated at room temperature, (a) Rietveld analyses of the BLZT0.08 sample exhibit excellent matching between the observed and calculated intensities, the inserted graph in (b) is a schematic structure diagram of tetragonal BLZT, (c) Transmission electron microscopy (TEM) images, and (d) their respective selected area electron diffraction (SAED) patterns of the BLZT0.08 ceramics.

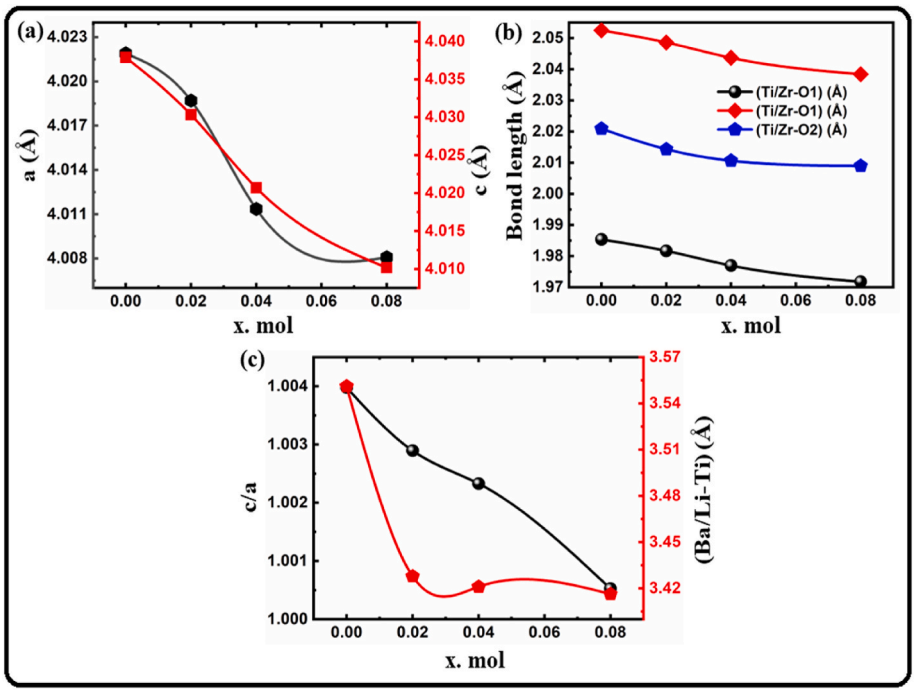

Fig. 2. (a) Variation of the lattice parameters (*a* and *c*) with Li concentrations, (b) variation of bonds length with Li content, and (c) a graphical represented the variation of tetragonality with Li concentrations in Li doped BZT ceramics.

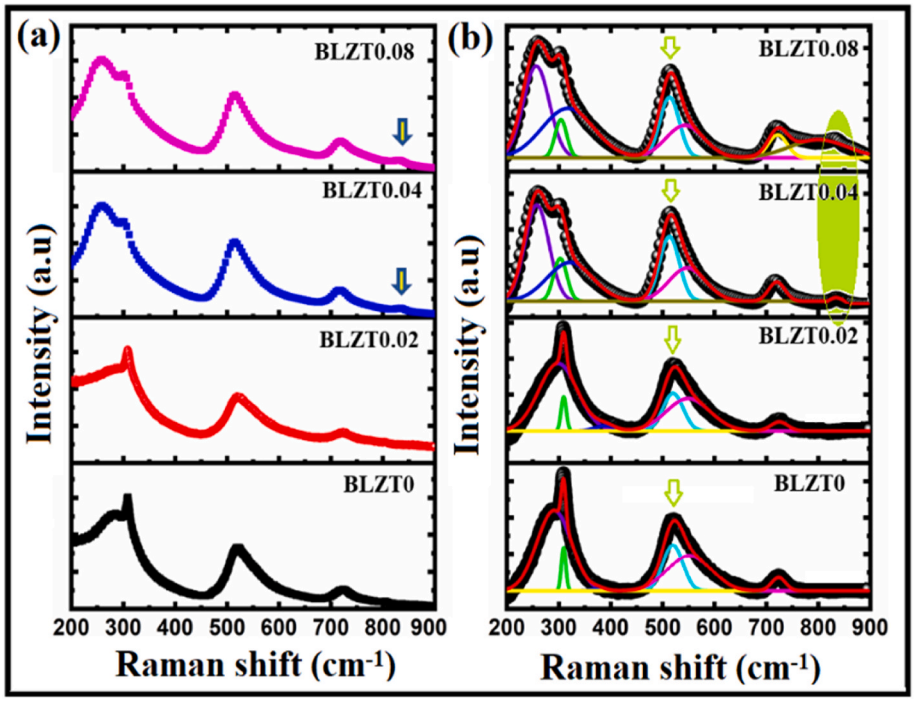

Fig. 3. (a) Raman spectra of all investigated samples, and (b) Deconvolution of Raman spectra, the black and red lines correspond to the experimental and deconvoluted curves, respectively.. (For interpretation of the references to colour in this figure legend, the reader is referred to the Web version of this article.)

the Ba-site caused most Raman modes to shift towards lower wavenumber, possibly due to octahedron distortion or Ti cation displacement [71–74]. It is easy to predict Raman mode shifting when an ion with a smaller/larger ionic radius, like Li^{+}-ions Li^{+}(0.73 Å) with 12- coordination replaces Ba^{2+}. One extra peak (A_1g) is detected at 800-820 cm^{-1} in the BLZT0.04 and BLZT0.08 samples, which is associated with the stretching mode of BO_6 octahedra, which becomes Raman active due to various B site species at the center of octahedra [75]. The appearance of this peak in the BLZT0.04 and BLZT0.08 samples may indicate relaxer-like behaviours, which may be attributed to the Ti vacancies created at B sites due to Li doping at A sites, which agrees with the literature reported by Kumar et al. [76,77].

The SEM micrographs of the sintered BLZT:x ceramics (x = 0, 0.02, 0.04 and 0.08) are summarized in Fig. 4. It can be observed that the

average grain size of BZT ceramics decreases with increasing Li^+ concentration. The average grain size of BLZT0, BLZT0.02, BLZT0.04, and BLZT0.08 is about 2.788 μm, 2.579 μm, 1.763 μm, and 1.078 μm, respectively. As the Li^+ content increased to 8%, the average grain size decreased to 1.078 μm, indicating that the Li^+ dopants can inhibit the growth of BZT ceramic grains. This inhabitation may be suggested that the Li^+ ions can incorporate with the BZT lattice and produce more oxygen vacancies by doping Li^+ with lower valence onto the Ba site. As a result of the formation of oxygen vacancies, defects were caused in the lattice. The defects interfere with the assembly of grains, thereby inhibiting crystal growth. Also, the decrease in grain size may be due to the grain growth restriction by resisting the grain boundary's mobility under the effect of Li^+ doping. We guess that the average grain sizes decreased also may be due to accumulated defects induced by Li doping along grain boundaries and impede grain growth. These observations are relevant to the previous literature work, where a strong Li enrichment over a wide range of GB widths is systematically observed for the GBs in the LLZO compound [78]. The decline could also be due to the variations in ionic mobility and increased crystal structure's deformation during the sintering process. The Defect induced via doping the Li^+ is beneficial for inhibiting grain growth and improving breakdown strength (Eb), as seen in the energy storage study section. In general, the E_b of a ceramic dielectric is highly correlated with its grain size (G), and it is also considered to follow an inverse power law ($E_b \propto G^{-1/2}$) [79,80]. Substantial effort has been put into reducing grains in dielectric ceramics so that the E_b can be improved.

XPS is an approach that can determine the different oxidation states of elements in their local chemistry. High-resolution XPS spectra of Ba 3d state, Zr 3d state, O1s state, Ti 2p state, and the Li 1s state of the $Ba_{0.92}Li_{0.08}Ti_{0.95}Zr_{0.05}O_3$ (BLZT:0.08) ceramic is represented in Fig. 5 (a), (b), (c), (d), and (e) respectively. Ba $3d_{5/2}$ and Ba $3d_{3/2}$ have binding energies of 778.14 and 793.42 eV, respectively, which agree well with other results [81]. Fig. 5(b) shows the Zr 3d XPS spectrum.

It is generally assumed that the peak at the lower binding energy, around 182.87 eV, is related to Zr $3d_{5/2}$, and the peak at the higher binding energy, around 185.33 eV, is related to Zr $3d_{3/2}$. The difference between Zr $3d_{5/2}$ and Zr $3d_{3/2}$ is approximately 2.46 eV, consistent with the literature reports [82]. Fig. 5(c) shows that the O 1s peaks contain two main peaks at around 529.23 eV, corresponding to oxygen in BZT, and a broad peak at 531.22 eV, which may represent chemical reaction between the surface and the adsorbate or oxygen vacancy [83] In Fig. 5 (d), you can see the XPS spectrum of Ti 2p. Peak spectra of Ti^{4+} $2p_{3/2}$ and Ti^{4+} $2p_{1/2}$ indicate that binding energies are found at 456.11 and 461,95 eV, respectively, and this is consistent with the binding energies reported for TiO_2 [84]. Further confirmation of the oxidation state of Ti^{4+} comes from the spin-orbital splitting energies between the Ti^{4+} $2p_{3/2}$ and Ti^{4+} $2p_{1/2}$ peaks being 5.84 eV. Two other signals were observed at binding energies of 455.33 and 460.11 eV, referred to as Ti^{3+} $2p_{3/2}$ and Ti^{3+} $2p_{1/2}$, respectively [84]. Ti^{3+} concentration [85] was estimated with the following formula and was found to be 49%

$$\left[Ti^{3+}\right] = \frac{Ti^{3+}_{Area}}{Ti^{3+}_{Area} + Ti^{4+}_{Area}} \quad (1)$$

As a result, it can be concluded that a significant amount of Ti^{3+} is present in Li doped BZT ceramics. In addition, this illustrates the impact of oxygen vacancies and Ti^{3+} defects on the ferroelectric properties of BLZT ceramics. This leads to defects dipoles [86], which pin domain walls and cause the hysteresis loop pinching, which leads to an improved energy storage efficiency, as we will see in the next section. As shown in Fig. 4(e), the peak associated with the Li 1s state is at 59.23 eV, associated with Li_2CO_3 [87].

Fig. 6 shows the dielectric constant and dielectric loss as a function of temperature for Li-doped BLZT ceramics measured at three different frequencies, namely 1 kHz, 100 kHz, and 1 MHz over the temperature range from 40 to 200 °C. From this figure, as the Li^+ ions increase the dielectric constant decreased and the Curie temperature shifted toward high temperatures with increase in frequency, which may indicate to their relaxor-like behaviours. Diffused phase transition has been observed in pure and Li doped BZT based ceramics. A possible explanation for this phenomenon may be related to the inhomogeneous distribution of ZrO_6 clusters at sites of Ti^{4+} [88]. According to literature the long-range polar ordering is disrupted by the size and charge differences caused by cation disorder [89]. Also, it can be seen in Table 2 and Fig. 6

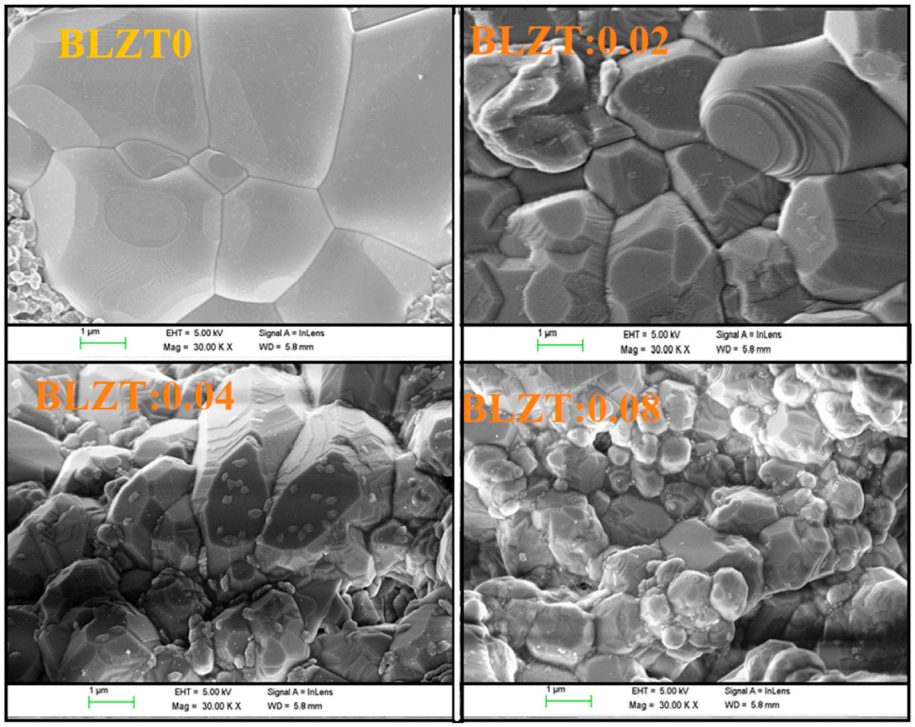

Fig. 4. Scanning Electron Microscopy (SEM) of BLZT:x ceramics.

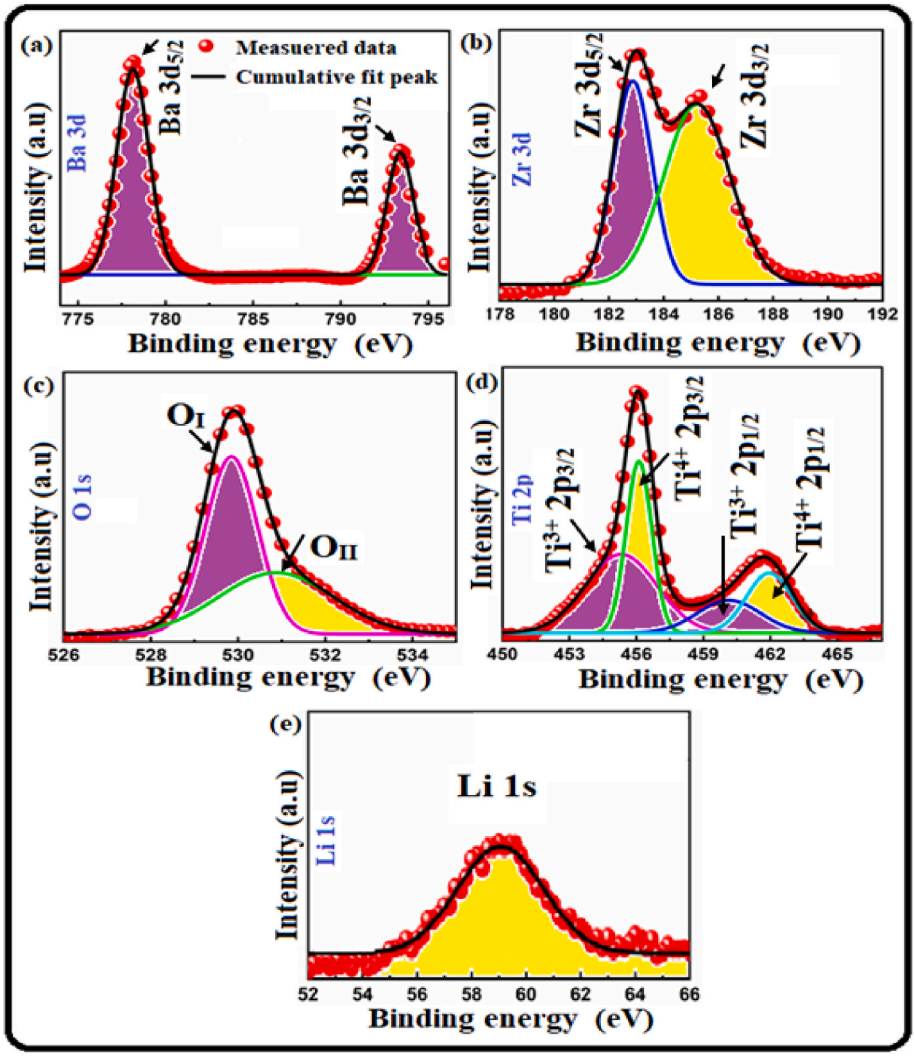

Fig. 5. High-resolution XPS spectra of (a) Ba 3d, (b) Zr 3d, (c) O 1s, (d) Ti 2p, and Li 1s for the $Ba_{0.92}Li_{0.08}Ti_{0.95}Zr_{0.05}O_3$ (BLZT:0.08) ceramic. The experimental signals are fitted with the Lorentzian equation.

that the dielectric permittivity decreases with increasing Li^+ concentration, which could be decrease in grain size. As we observed from the SEM images that the grain size decreases with the increase of the Li^+ content, which may be the reason for the decrease in dielectric permittivity. Jiang and Bursill et al. [90] proposed that the decrease in dielectric permittivity takes place as the grain size decrease due to the suppression of dipole polarization. To investigate the diffuseness of the phase transition in Li doped BZT the modified Curie-Weiss law can be used [91]:

$$\frac{1}{\varepsilon}-\frac{1}{\varepsilon_m}=\frac{(T-T_m)^{\gamma}}{C_1} \quad (2)$$

Where γ is the degree of diffuseness that gives the information about the diffused phase transition of the investigated samples. The inserted graphs in Fig. 6, exhibits the relationship between the $\ln(1/\varepsilon\text{-}1/\varepsilon_m)$ and $\ln(T\text{-}T_m)$ above the Curie temperature region at 1 kHz. The degree of diffuseness is estimated from the slope of the plotted curves.

The γ varies from 1 to 2, suggesting that the samples are somewhat a typical relaxor-like behaviour. The relaxor-like behaviour in the BLZT0.08 sample may affect by several factors, such as changes in the microscopic composition, the merging of micro- and macro-polar regions, and the coupling of order parameters and local disorder modes via local strain [92,93]. Also, because of the inhomogeneous distribution of Li^+ ions in Ba^{2+} and Zr^{4+} ions in Ti^{4+} sites, the doped BLZT bulk ceramic exhibit high diffused around the phase transition temperatures. On the other hand, a higher value of diffusiveness may be attributed to the small grain size and large grain boundary numbers. The delicate balance between the long-range and short-range forces, which determines the relaxor state, is therefore thought to be changed by a reduction in grain size [94]. Essentially, diffuse phase transitions (relaxor-like behaviour) exhibit slim ferroelectric loops that can play an essential role in improving energy storage properties, as seen in the following sections.

Impedance spectroscopy measurements for BLZTx ceramics are shown in Fig. 7. A semi-circular is observed in doped samples to indicate that the doped samples electrically behave as an RC circuit network and present a single relaxation process and was used to estimate the behaviour of bulk resistivity. A sample was prepared in the shape of pellets with a thickness of 0.5 mm and a surface area around A = 65 mm^2. Silver was used for the preparation of electrodes. Based on the grain resistance obtained from Cole-Cole plots and geometric parameters mentioned above, the bulk resistivity of BLZTx samples was estimated using the formula [95]:

$$\rho = R_g\frac{A}{l} \quad (3)$$

The obtined parameters are listed in Table 2. It is noted that there is an apparent decrease in bulk resistivity with an increase in the Li-doping concentration, which could be due to an increase in the defects. The

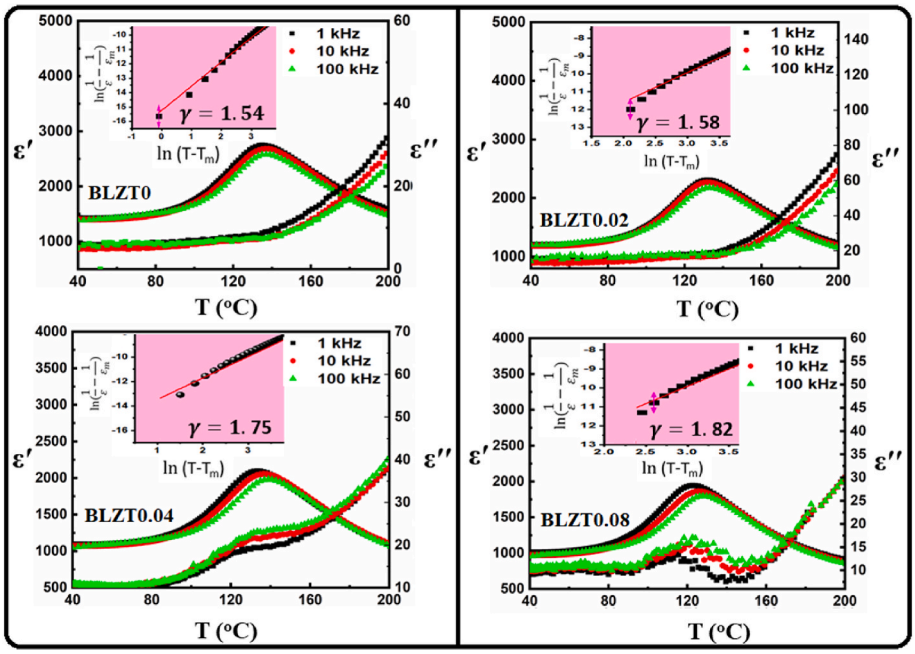

Fig. 6. **(a)** The temperature dependence of dielectric constant measured at 1 kHz, and the inserted graphs represented the linear fitting of the modified Curie–Weiss law above Curie temperature (Tc) of BLZTx ceramics at 1 kHz, and the estimated values of the degree of diffuseness are inserted in graphs.

Table 2
Dielectric constant at Curies temperature, Curie temperature, Curie constant, Cole-Cole plot output data, Remnant polarization, maximum polarization, breakdown voltage, recoverable energy.

Sample	BLZT0	BLZT0.02	BLZT0.04	BLZT0.08
Dielectric constant @ Tc	2753	2303	2106	1947
Curie Temperature (°C)	134.8	132	132	121
$Rg \times 10^6$ Ω	10.99	10.25	09.05	08.25
$\rho \times 10^8$ (Ω cm)	1.4287	1.3325	1.1765	1.0725
$Cg \times 10^{-5}$ (F)	10	13.71	14.562	17.35
P_{max} (μC/cm^2)	14.81	13.88	12.55	13.22
P_r (μC/cm^2)	8.30	2.89	1.60	0.754
E_b (kV/cm)	97.5	117.64	124.2	138.25
W_{rec} (J/cm^3)	0.191	0.452	0.593	0.701
η (%)	7	51	57	81

semicircle impedance spectrum may refer to relaxor-like behaviour [96]. The relaxor-like behaviour in the investigated sample has been evaluated using the Raman study, as seen in the Raman discussion.

Capacitors in electronic equipment are designed to store electric energy. Capacitance, defined by the capacitor's physical geometry and the dielectric materials' permittivity, is the capacity to store energy. The charging process occurs at the electrodes of dielectric capacitors when they are exposed to an external electric field and have opposite signs and equal magnitude charges. In opposition to the external electric field, the charges create a local electric field. The accumulated charge builds up as the internal electric field grows. The charging process is complete when the internal electric field produced by the built-up charges equals the external field. The charges drift under the externally provided electric field during the charging process. The energy-storage density (W) is essential for examining dielectric capacitors' energy-storage performance.

There are two ways to describe the energy-storage density (W) of the dielectric capacitors. Integrating the curve between the polarization axis and the electric field axis (also known as *P-E* loops) is the most frequent method, as shown in Fig. 8(a). The red-shaded area represents the recoverable energy density (W_{rec}) or the released energy density during the discharge process. The yellow shaded area represents the energy loss (Wloss) that occurs throughout the charge-discharge process. (W_{rec}) plus (W_{loss}) represents the overall energy density (W_{total}) stored during the charging process. Mathematically the energy storage parameters can be described by the following equations [97]:

$$W = \int_0^{P_{max}} Edp \tag{4}$$

$$W_{rec} = \int_{P_r}^{P_{max}} Edp \tag{5}$$

$$W_{loss} = W - W_{rec} \tag{6}$$

$$\eta = \frac{W_{rec}}{W_{rec} + W_{loss}} \tag{7}$$

where P_r denotes the remnant polarization, P_{max} denotes the maximum polarization, and E is the applied electric field. The obtined parameters are listed in Table 2. The above equations indicate that the high P_{max}, low P_r, and high E_b can achieve higher energy storage density and energy storage efficiency in the dielectric materials. There are two alternative mechanisms to increase the energy storage density of BZT ceramics for energy storage applications. The first boosts breakdown strength (*BDS*), and the second creates a significant difference between P_{max} and P_r [98]. To further explore the origin of the defects-induced effect, the *P-E* hysteresis loop was investigated at a frequency of 10 Hz, as shown in Fig. 8(a). The as-doped BZT shows slim hysteresis loops at room temperature (typical of relaxor-like behaviour). Upon increasing the Li-concentration, the breakdown strength (*BDS*) of the hysteresis loop increases from 98 kV cm^{-1} at x = 0–138 kV cm^{-1} at x = 0.08. The significant rise of the breakdown electric field was believed to have resulted from the decreasing in grain size with increase Li^+ content. According to SEM images of the BLZT0.08 sample, an exponential decline relationship with grain size [99] suggests that the smallest grain size considerably contributes to the enhanced breakdown strength E_b. A change in the shape of hysteresis loops is apparent with an increase in Li-content. A pinching appears in the hysteresis loops and becomes more pronounced as the Li-content increased [Fig. 8(a)]. The pinching of the hysteresis loops is the signature of the formation of defect dipoles (i.e., complex defects composed of point defects of opposite charge) in the

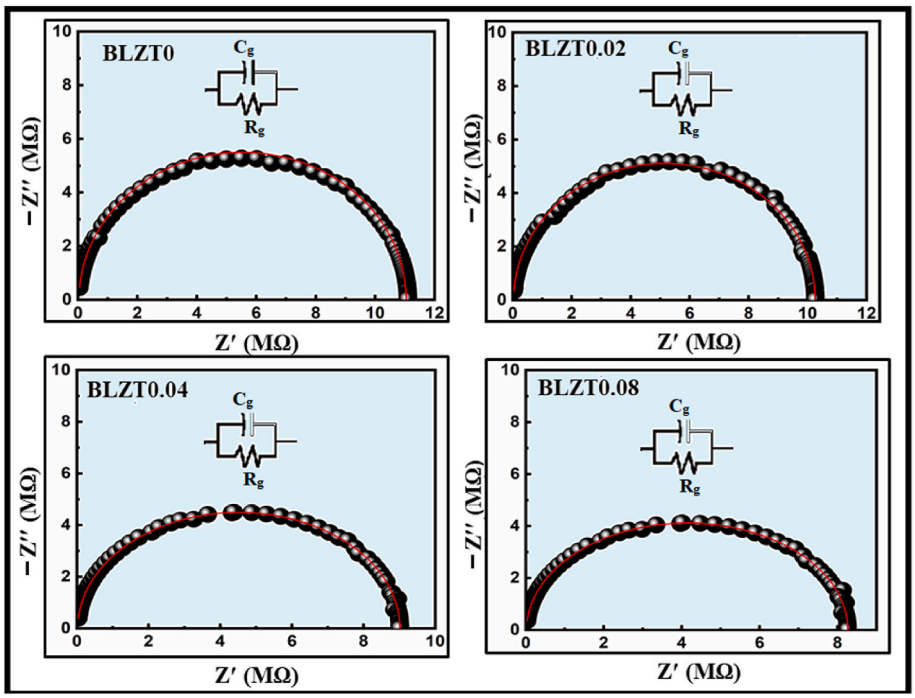

Fig. 7. Cole-Cole plot of the BLZT:x ceramics measured at room temperature.

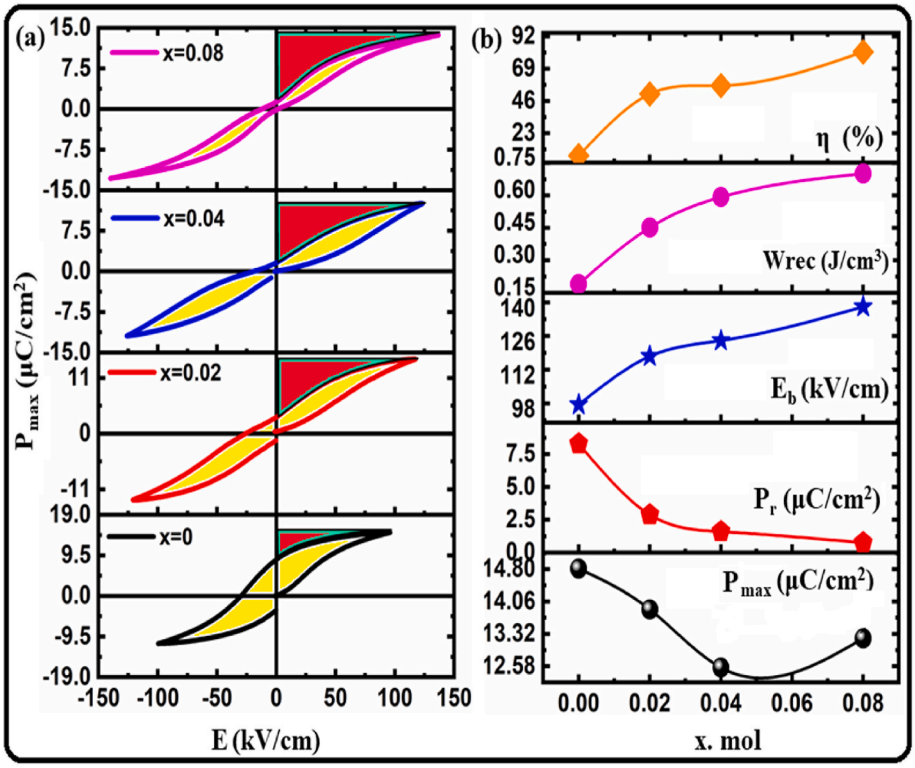

Fig. 8. (a) Displays the bipolar P-E loops of Li-doped BZT ceramics measured at room temperature and a frequency of 10 Hz, while (b) illustrates the relationship between maximum polarization (P_{max}), remnant polarization (P_r), maximum applied field (E_b), recoverable energy density (W_{rec}), and energy storage efficiency (η) with Li-doping concentrations (x).

BLZTx, similar to effects observed in other polar systems [100–102]. Remarkably, the doping of an acceptor ion can cause a defective dipole. Literature suggests that these defect dipoles can create a dipole moment (P_d), which may act as an internal field when an electric field is removed, causing the domain to return to its original state resulting in pinching the hysteresis loop [100–102]. By increasing the Li ions, the defect dipoles increase, causing more pronounced pinching of the hysteresis loops. These defects can limit the rotation of spontaneous polarization. According to the domain-wall effect model, defects, defect dipoles, or oxygen vacancies "pin" the domain wall, which acts as an

energy barrier to the domain-wall motion in ferroelectrics [102–105]. Defect dipoles (P_d) typically align in the polarization direction and act as pinning centres for polarization switching in its host domain. When the applied electric field decrease, the P_d, which maintains its original orientation, will provide a restoring force that forces P_s to return to their original state [106,107]. As a result, the remnant polarization of BLZTx ceramics would significantly decrease. Thus, the *P-E* loops get pinched, as shown in the schematic diagram in Fig. 9. This phenomenon will create a high difference between the P_s and P_r. On another side, the increase of Li-content leads to a decrease in the grain size, which results in enhanced breakdown strength so that these two parameters (High difference between P_s and P_r) and high breakdown strength (E_b) will lead to increased energy storage density and high energy storage efficiency.

It is generally known that when ceramics are doped with acceptor atoms, oxygen vacancies are introduced by valence compensation. The oxygen vacancies and acceptor atom Li^+ then combine to generate complex defects. These defects naturally serve as domain rotation pinning sites, pinching the hysteresis loop in the end. These types of complex defects and their effect on domain switching are discussed earlier by our group [108,109]. Complex defects have been demonstrated to have a smaller coercive field than the defect-free case. We evaluated the *P-E* hysteresis loop of the BLZT0.08 sample before and after immediate poling to acquire clear proof of the complex defects. The resulting data are depicted in Fig. 10. After poling at a high applied field (9 kV/mm) for 1 h, the sample showed an increase in its remnant polarization and coercive field, in contrast to what was observed for the sample before poling. It has been confirmed that the sample BLZT0.08 without poling exhibited a pinching hysteresis loop that was consistent with the reported behaviour given by Takahashi [55]. This fact is linked to the complex defects that impede domain rotation [55,61].

The comparison shows that the energy storage density of BLZT0.08 ceramics is 0.701 J/cm^3 and the energy storage efficiency is 81%, which is much better than other samples under investigation. Fig. 8(b) shows that the high energy storage density is linked with high values of P_{max} and breakdown strength E_b. Therefore, this sample was considered one of the best samples in our study, so to investigate its stability, we subjected it to different temperatures and frequencies. It is well known that one of the critical requirements for energy storage devices is temperature stability. At $f = 10$ Hz and $E = 130$ kV/cm, the unipolar *P-E* loops were measured over the temperature range of 30–100 °C, as shown in Fig. 11(a). As can be seen, the P_{max} practically remains steady across the examined temperature range. The corresponding W_{rec} and η values are unchanged. Additionally, as demonstrated in Figures, 11 (b), both W_{rec} and η values exhibit good stability with frequency in the range of (5 Hz–1 kHz).

4. Conclusions

In summary, we have studied the effect of acceptor ions such as Li-doped BZT ceramics on the structural, dielectric, ferroelectric, and energy storage properties. We consider the defect dipoles created on the BZT lattice to be the reason for the hardening nature of the BZT ferroelectric ceramics due to the pining effects on the ferroelectric domains. This study showed one attractive approach to improving energy storage density and energy storage efficiency by creating defect dipoles on the (BZT) host lattice. The results showed that the defect dipole interacted with the spontaneous polarization in its host domains, leading to pinching the *P-E* loop. Accordingly, during a *P-E* loop measurement at 10 Hz frequency, the P_d will maintain its original orientation and prevent the P_s from switching, resulting in higher electric fields in the stabilized domain. This results in a significant reduction in remnant polarization. Therefore, the polarization loops on acceptor-doped piezoelectric ceramics have "pinched" shapes, affecting the energy storage properties. The BLZT0.08 sample was shown thermal stability over a range of temperatures, making them a good candidate for applications in the field of energy storage. Improving energy storage density and efficiency by forming defect dipoles in ferroelectric host-lattice is one of the attractive approaches to enhancing ferroelectric materials for energy storage applications.

CRediT authorship contribution statement

Mahmoud S. Alkathy: Synthesized, analyzed, and interpreted data,

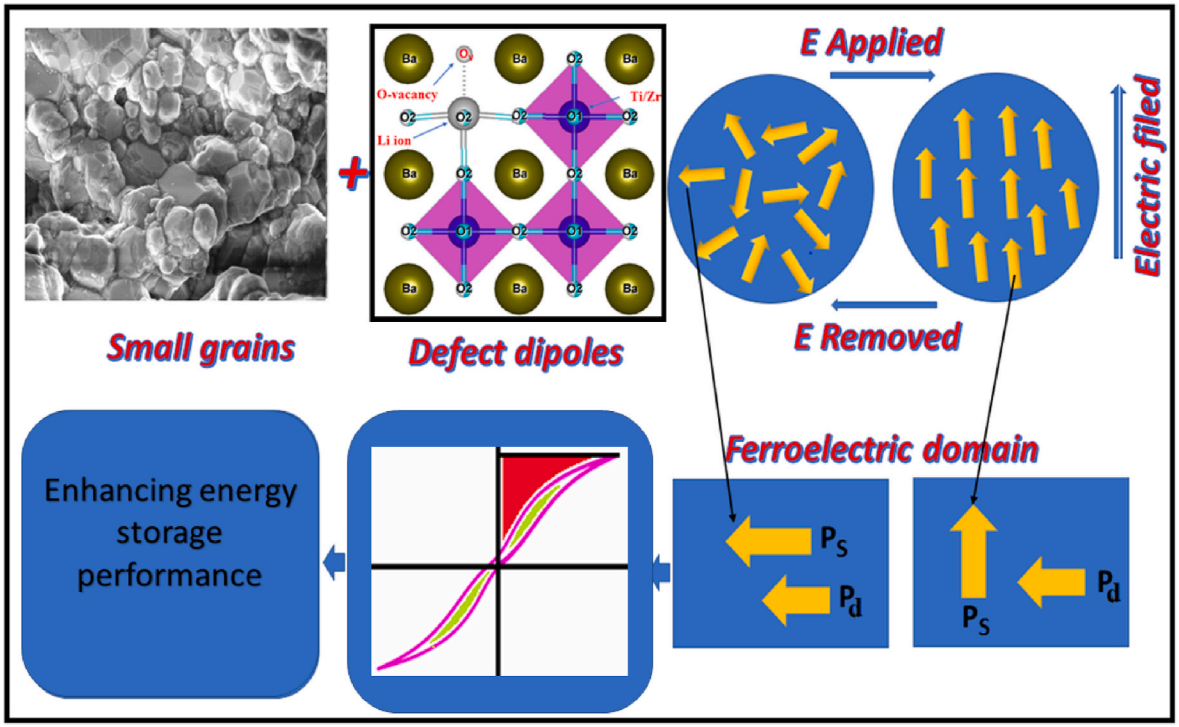

Fig. 9. A schematic diagram illustrates how defect dipoles cause a pinching *P-E* hysteresis loop, which results in a high energy storage density.

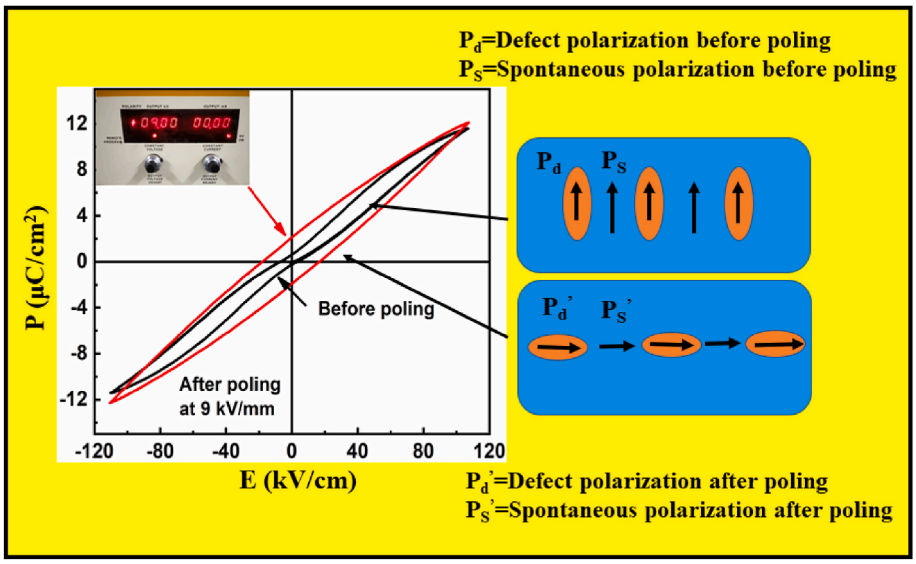

Fig. 10. (a) Hysteresis loops for the BLZT0.08 measured before (black curve) and immediately after being poling (red curve), and (b) the corresponding schematic diagram of domain switching before and after poling process. (For interpretation of the references to colour in this figure legend, the reader is referred to the Web version of this article.)

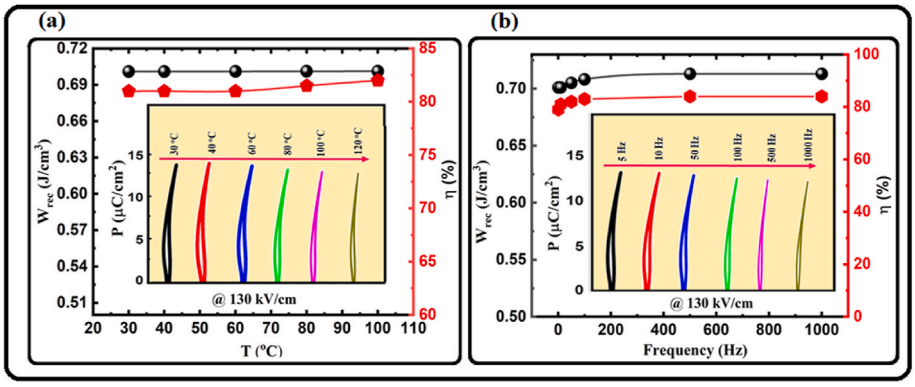

Fig. 11. Shows (a) Unipolar *P-E* loops of the BLZT0.08 ceramic measured at different temperatures at 130 kV/cm and 10 Hz frequency, also the corresponding W_{rec} and η values, while (b) Unipolar *P-E* loops of the BLZT0.08 ceramic measured at various frequencies at ambient temperature, with corresponding W_{rec} and η values.

calculations, Visualization, Conceptualization, Methodology, Writing – original draft. **Attaur Rahaman:** Investigation. **Valmor R. Mastelaro:** Investigation, and XPS measurements. **Flavio Paulo Milton:** Investigation, and hysteresis loop measurements. **Fabio L. Zabotto:** Investigation. **Manuel H. Lente:** Conceptualization, suggestions. **Alexandre Strabello:** Investigation. **J.A. Eiras:** Supervision, validated, wrote, reviewed, and approved the final version. All authors have contributed to the preparation of the manuscript.

Declaration of competing interest

The authors declare that they have no known competing financial interests or personal relationships that could have appeared to influence the work reported in this paper.

Data availability

The data that has been used is confidential.

Acknowledgements

The authors would like to acknowledge the experimental facilities provided by CNPq and FAPESP in Grupo de Materiais Ferroicos (GMF), Physics Department/UFSCar. For financial support, Prof. Dr. Eiras, Dr Alkathy and Dr. Atta are greatly indebted to the Sao Paulo Research Foundation FAPESP: (Grant no. 2017/13769-1), (Grant no. 2019/03110-8), and (Grant no. 2022/00821-3) respectively.

References

[1] Sam Koohi- Kamali, V.V. Tyagi, N.A. Rahim, N.L. Panwar, H. Mokhlis, Emergence of energy storage technologies as the solution for reliable operation of smart power systems: a review, Renew. Sustain. Energy Rev. 25 (2013) 135–165.
[2] Bikesh Gupta, Md Anower Hossain, Asim Riaz, Astha Sharma, Doudou Zhang, Hark Hoe Tan, Chennupati Jagadish, Kylie Catchpole, Bram Hoex, Siva Karuturi, Recent advances in materials design using atomic layer deposition for energy applications, Adv. Funct. Mater. 3 (2022), 2109105.
[3] F. Wu, L. Liu, S. Wang, J.R. Xu, P.S. Lu, W.L. Yan, J. Peng, D.X. Wu, H. Li, Solid state ionics - selected topics and new directions, Prog. Mater. Sci. 126 (2022), 100921.
[4] Yu Li, Zheng-Yi Fu, Bao-Lian Su, Hierarchically structured porous materials for energy conversion and storage, Adv. Funct. Mater. 22 (22) (2012) 4634–4667.
[5] N. Wei, L. Yu, Z. Sun, Y. Song, M. Wang, Z. Tian, Y. Xia, J. Cai, Y.Y. Li, L. Zhao, Q. Li, Scalable salt-templated synthesis of nitrogen-doped graphene nanosheets toward printable energy storage, ACS Nano 13 (7) (2019) 7517–7526.
[6] Christopher Choi, David S. Ashby, Danielle M. Butts, Ryan H. DeBlock, Qiulong Wei, Jonathan Lau, Bruce Dunn, Achieving high energy density and high-power density with pseudocapacitive materials, Nat. Rev. Mater. 5 (1) (2020) 5–19.
[7] Guiwei Yan, Liqin Xu, Bijun Fang, Shuai Zhang, Xiaolong Lu, Xiangyong Zhao, Jianning Ding, Achieving high pulse charge–discharge energy storage properties

and temperature stability of $(Ba_{0.98-x}Li_{0.02}La_x)(Mg_{0.04}Ti_{0.96})O_3$ lead-free ceramics via bandgap and defect engineering, J. Chem. Eng. 450 (2022), 137814.
[8] J. Li, Z. Shen, X. Chen, et al., Grain-orientation-engineered multilayer ceramic capacitors for energy storage applications, Nat. Mater. 19 (2020) 999–1005.
[9] Yizhou Wang, Tianchao Guo, Jian Yin, Zhengnan Tian, Yinchang Ma, Zhixiong Liu, Yunpei Zhu, N. Husam, Alshareef. Controlled deposition of zinc-metal anodes via selectively polarized ferroelectric polymers, Adv. Mater. 34 (4) (2022), 2106937.
[10] Arindam Dutta, Shirsendu Mitra, Mitali Basak, Tamal Banerjee, A comprehensive review on batteries and supercapacitors: development and challenges since their inception, Energy Storage (2022) e339.
[11] Hong Wei Tan, Yu Ying Clarrisa Choong, Che Nan Kuo, Yee Hong, Low, Chee Kai Chua, 3D printed electronics: processes, materials and future trends, Prog. Mater. Sci. 127 (2022), 100945.
[12] M. Pershaanaa, S. Shahid Bashir, Ramesh, K. Ramesh, Every bite of Supercap: a brief review on construction and enhancement of supercapacitor, J. Energy Storage 50 (2022), 104599.
[13] Ke Bi, Meihua Bi, Hao Yanan, Wei Luo, Ziming Cai, Xiaohui Wang, Yunhui Huang, Ultrafine core-shell $BaTiO_3$@ SiO_2 structures for nanocomposite capacitors with high energy density, Nano Energy 51 (2018) 513–523.
[14] A.S. Bhalla, Ruyan Guo, Rustum Roy, The perovskite structure—a review of its role in ceramic science and technology, Mater. Res. Innovat. 4 (1) (2000) 3–26.
[15] E.A.R. Assirey, Perovskite synthesis, properties and their related biochemical and industrial application, SPJ 27 (6) (2019) 817–829.
[16] Priyanshu Goel, Shashank Sundriyal, Vishal Shrivastav, Sunita Mishra, Deepak P. Dubal, Ki-Hyun Kim, Akash Deep, Perovskite materials as superior and powerful platforms for energy conversion and storage applications, Nano Energy 80 (2021), 105552.
[17] T. Mikolajick, S. Slesazeck, H. Mulaosmanovic, M.H. Park, S. Fichtner, P. D. Lomenzo, M. Hoffmann, U. Schroeder, Next generation ferroelectric materials for semiconductor process integration and their applications, J. Appl. Phys. 129 (2021), 100901.
[18] H. Zhao, X. Yang, D. Pang, X. Long, Enhanced energy storage efficiency by modulating field-induced strain in $BaTiO_3$-$Bi(Ni_{2/3}Ta_{1/3})O_3$ lead-free ceramics, Ceram. Int. 47 (16) (2021) 22734–22740.
[19] Mahmoud S. Alkathy, J.A. Eiras, K.C. James Raju, Energy storage enhancement and bandgap narrowing of lanthanum and sodium co-substituted $BaTiO_3$ ceramics, Ferroelectrics 570 (1) (2021) 153–161.
[20] Mahmoud S. Alkathy, KC James Raju, J.A. Eiras, Colossal dielectric permittivity and high energy storage efficiency in barium strontium titanate ceramics co-doped with bismuth and lithium, J. Phys. D Appl. Phys. 54 (12) (2021), 125501.
[21] H. Ye, F. Yang, Z. Pan, D. Hu, X. Lv, H. Chen, F. Wang, J. Wang, P. Li, J. Chen, J. Liu, Significantly improvement of comprehensive energy storage performances with lead-free relaxor ferroelectric ceramics for high-temperature capacitors applications, Acta Mater. 203 (2021), 116484.
[22] Ziyu Zhang, Tao Ding, Quan Zhou, Yuge Sun, Ming Qu, Ziyu Zeng, Yuntao Ju, Li Li, Kang Wang, Fangde Chi, A review of technologies and applications on versatile energy storage systems, Renew. Sustain. Energy Rev. 148 (2021), 111263.
[23] P. Zhao, Z. Fang, X. Zhang, J. Chen, Y. Shen, X. Zhang, Q. An, C. Yang, X. Gao, S. Zhang, B. Tang, Aliovalent doping engineering for A-and B-sites with multiple regulatory mechanisms: a strategy to improve energy storage properties of $Sr_{0.7}Bi_{0.2}TiO_3$-based lead-free relaxor ferroelectric ceramics, ACS Appl. Mater. Interfaces 13 (21) (2021) 24833–24855.
[24] Shuaishuai Ji, Qianjie Li, Dongdong Wang, Jiangyuan Zhu, Min Zeng, Zhipeng Hou, Zhen Fan, et al., Enhanced energy storage performance and thermal stability in relaxor ferroelectric $_{(1-x)}BiFeO_3$-x$(0.85BaTiO_{3-0.15}Bi(Sn_{0.5}Zn_{0.5})O_3)$ ceramics, J. Am. Ceram. Soc. 104 (6) (2021) 2646–2654.
[25] Nengneng Luo, Xinya Tang, Kai Han, Li Ma, Zhenpei Chen, Xiyong Chen, Feng Qin, Changzheng Hu, Yuezhou Wei, Toyohisa Fujita, Silver stoichiometry engineering: an alternative way to improve energy storage density of $AgNbO_3$-based antiferroelectric ceramics, J. Mater. Sci. Res. 36 (5) (2021) 1067–1075.
[26] J. Wang, X. Nie, Z. Peng, X. Lei, P. Liang, Z. Yang, X. Chao, Ultra-fast charge-discharge and high energy storage density realized in $NaNbO_3$–$La(Mn_{0.5}Ni_{0.5})O_3$ ceramics, Ceram. Int. 47 (20) (2021) 28493–28499.
[27] G. Wang, Z. Lu, Y. Li, L. Li, H. Ji, A. Feteira, D. Zhou, D. Wang, S. Zhang, I. M. Reaney, Electroceramics for high-energy density capacitors: current status and future perspectives, Chem. Rev. 121 (10) (2021) 6124–6172.
[28] F. Yan, Y. Shi, X. Zhou, K. Zhu, B. Shen, J. Zhai, Optimization of polarization and electric field of bismuth ferrite-based ceramics for capacitor applications, Chem. Eng. J. 417 (2021), 127945.
[29] Satyanarayan Patel, Aditya Chauhan, Rahul Vaish, P. Thomas, Enhanced energy storage performance of glass added $0.715Bi_{0.5}Na_{0.5}TiO_3$-$0.065BaTiO_{3-0.22}SrTiO_3$ ferroelectric ceramics, J. Asian Ceram. Soc. 3 (4) (2015) 383–389.
[30] Peng Wang, Xusheng Wang, Guorong Li, Rui Hu, Kun Zhu, Yanxia Li, Xi Yao, Zhongbin Pan, Nanocrystalline engineering induced high energy storage performances of fatigue-free $Ba_2Bi_{3.9}Pr_{0.1}Ti_5O_{18}$ ferroelectric thin films, ACS Appl. Mater. Interfaces 14 (15) (2022) 17642–17651.
[31] Xue-Jie Liu, Ming-Sheng Zheng, Gang Wang, Yiyi Zhang, Zhi-Min Dang, George Chen, Jun-Wei Zha, High energy density of polyimide films employing imidization reaction kinetics strategy at elevated temperature, J. Mater. Chem. A. 10 (2022) 10950–10959.
[32] Sergey I. Shkuratov, Christopher S. Lynch, A review of ferroelectric materials for high power devices, J Materiomics 8 (4) (2022) 739–752.
[33] Julia A. Mundy, Bastien F. Grosso, Colin A. Heikes, Dan Ferenc Segedin, Zhe Wang, Yu-Tsun Shao, Dai Cheng, et al., Liberating a hidden antiferroelectric phase with interfacial electrostatic engineering, Sci. Adv. 8 (5) (2022), eabg5860.
[34] Jiayi He, Xiao Liu, Yingying Zhao, Huiling Du, Tao Zhang, Jing Shi, Dielectric stability and energy-storage performance of BNT-based relaxor ferroelectrics through Nb^{5+} and its excess modification, ACS Appl. Electron. Mater. 4 (2) (2022) 735–743.
[35] X. Chen, H. Qin, X. Qian, W. Zhu, B. Li, B. Zhang, W. Lu, R. Li, S. Zhang, L. Zhu, Relaxor ferroelectric polymer exhibits ultrahigh electromechanical coupling at low electric field, Science 375 (6587) (2022) 1418–1422.
[36] Xinyi Du, Yongping Pu, Xin Peng, Jinbo Zhang, Jiamin Ji, Run Li, Qianwen Zhang, Min Chen, Optimizing the energy storage and charge-discharge performance of borate glass-ceramics by adjusting the glass structure, Ceram. Int. 48 (4) (2022) 5404–5412.
[37] L. Wu, B. Luo, E. Tian, Ferroelectric properties of $BaTiO_3$-$BiScO_3$ weakly coupled relaxor energy-storage ceramics from first-principles calculations, J. Alloys Compd. 866 (2021), 158933.
[38] M. Khalid Hossain, Gazi A. Raihan, Md Ali Akbar, Mirza Humaun Kabir Rubel, Mohammad Hafez Ahmed, Md Ishak Khan, Shahadat Hossain, Sapan Kumar Sen, M.I.E. Jalal, A. El-Denglawey, Current applications and future potential of rare earth oxides in sustainable nuclear, radiation, and energy devices: a review, ACS Appl. Electron. Mater. 4 (7) (2022) 3327–3353.
[39] Kaikai Chen, Hairui Bai, Fei Yan, He Xia, Changshuai Liu, Shufeng Xie, Bo Shen, Jiwei Zhai, Achieving superior energy storage properties and ultrafast discharge speed in environment-friendly niobate-based glass ceramics, ACS Appl. Mater. Interfaces 13 (3) (2021) 4236–4243.
[40] Xinyi Du, Yongping Pu, Xin Li, Xin Peng, Zixiong Sun, Jinbo Zhang, Jiamin Ji, Run Li, Qianwen Zhang, Min Chen, Optimizing the energy storage performance of K_2O–Nb_2O_5–SiO_2 based glass-ceramics with excellent temperature stability, Ceram. Int. 47 (7) (2021) 8987–8995.
[41] Xiaoyan Dong, Li Xu, Xiuli Chen, Jiagang Wu, Huanfu Zhou, Simultaneous enhancement of polarization and breakdown strength in lead-free $BaTiO_3$-based ceramics, Chem. Eng. J. 409 (2021), 128231.
[42] J. Hu, Y. Liu, S.F. Zhang, B.T. Tang, Novel designed core-shell nanofibers constituted by single element-doped $BaTiO_3$ for high-energy-density polymer nanocomposites, Chem. Eng. J. 428 (2022), 131046.
[43] Wenfeng Liu, Yi Zhao, Yihang Jin, Fanyi Kong, Jinghan Gao, Shengtao Li, Enhanced dielectric tunability and reduced dielectric loss in the La/Fe co-doped $Ba_{0.65}Sr_{0.35}TiO_3$ ceramics, J. Alloys Compd. 901 (2022), 163642.
[44] Huanghui Nie, Limei Ruan, Lu Hu, Xinran Wang, Fukang Chen, Shuai Zhou, Yangyang Wang, Taotao Ai, Yan Yan, Gang Liu, Enhanced dielectric energy storage performance of A-site Ca^{2+}-doped $Na_{0.5}Bi_{0.5}TiO_3$–$BaTiO_3$–$BiFeO_3$ Pb-free ceramics, Ceram. Int. 48 (15) (2022) 21061–21070.
[45] Qi-Guo Hu, Zong-Yang Shen, Yue-Ming Li, Zhu-Mei Wang, Wen-Qin Luo, Zhi-Xiang Xie, Enhanced energy storage properties of dysprosium doped strontium titanate ceramics, Cerm. Int. 40 (1) (2014) 2529–2534.
[46] Xiaoyan Dong, Li Xu, Xiuli Chen, Hongyun Chen, Congcong Sun, Junpeng Shi, Feihong Pang, Huanfu Zhou, High energy storage density and power density achieved simultaneously in $NaNbO_3$-based lead-free ceramics via antiferroelectricity enhancement, J Materiomics 7 (3) (2021) 629–639.
[47] M.S. Alkathy, A. Rahaman, V.R. Mastelaro, F.L. Zabotto, F.P. Milton, J.A. Eiras, Achieving high energy storage density simultaneously with large efficiency and excellent thermal stability by defect dipole, and microstructural engineering in modified-$BaTiO_3$ ceramics, J. Alloys Compd. 934 (2022), 167887.
[48] Aditya Jain, Y.G. Wang, H. Guo, Significant enhancement in microstructural and electrical properties of lead-free $_{(1-x)}$ $Ba_{0.9}Sr_{0.1}Ti_{0.9}Zr_{0.1}O_{3-x}LiNbO_3$ ceramic composites, J. Alloys Compd. 857 (2021), 158244.
[49] N. Narayanan, Q. Lou, A. Rawal, T. Lu, Z. Liu, J. Chen, J. Langley, H. Chen, J. Hester, N. Cox, H. Fuess, G.J. McIntyre, G. Li, D. Yu, Y. Liu, Defect structure and property consequence when small Li^+ ions meet $BaTiO_3$, Phys. Rev. Mater. 4 (8) (2020), 084412.
[50] Gui-wei Yan, Ming-gang Ma, Cheng-bo Li, Zhi-wei Li, Xiao-yu Zhong, Jian Yang, Fei Wu, Zhi-hui Chen, Enhanced energy storage property and dielectric breakdown strength in Li^+ doped $BaTiO_3$ ceramics, J. Alloys Compd. 857 (2021), 158021.
[51] M.S. Alkathy, R. Gayam, K.C. James Raju, Effect of sintering temperature on structural and dielectric properties of Bi and Li co-substituted barium titanate ceramic, Ceram. Int. 42 (2016) 15432–15441.
[52] H.B. Yang, P.F. Liu, F. Yan, Y. Lin, T. Wang, A novel lead-free ceramic with layered structure for high energy storage applications, J. Alloys Compd. 773 (2019) 244–249.
[53] M.S. Alkathy, Fabio L. Zabotto, KC James Raju, J.A. Eiras, Effect of defects on the band gap and photoluminescence emission of Bi and Li co-substituted barium strontium titanate ceramics, Mater. Chem. Phys. 275 (2022), 125235.
[54] Qi Wang, Tongtong Wang, Ling Zhang, Zhiyong Liu, Kun Guo, Jinshan Lu, Bing Xie, High energy-storage performance of lead-free $Ba_{0.4}Sr_{0.6}TiO_3$–$Sr_{0.7}Bi_{0.2}TiO_3$ relaxor-ferroelectric ceramics with ultrafine grain size, Ceram. Int. 48 (2) (2022) 2068–2074.
[55] Ulrich Weber, Georg Greuel, Boettger Ulrich, Sophie Weber, Detlev Hennings, Rainer Waser, Dielectric properties of $Ba(Zr,Ti)O_3$-based ferroelectrics for capacitor applications, J. Am. Ceram. Soc. 84 (4) (2001) 759–766.
[56] S. Takahashi, Effects of impurity doping in lead zirconate-titanate ceramics, Ferroelectrics 41 (1) (1982) 143–156.
[57] P.V. Lambeck, G.H. Jonker, Ferroelectric domain stabilization in $BaTiO_3$ by bulk ordering of defects, Ferroelectrics 22 (1978) 729.

[58] W.L. Warren, G.E. Pike, K. Vanheusden, D. Dimos, B.A. Tuttle, Defect-dipole alignment and tetragonal strain in ferroelectrics, J. Appl. Phys. 79 (1996) 9250.
[59] W.L. Warren, D. Dimos, G.E. Pike, K. Vanheusden, R. Ramesh, Alignment of defect dipoles in polycrystalline ferroelectrics, Appl. Phys. Lett. 67 (1995) 1689.
[60] M.H. Lente, J.A. Eiras, Interrelationship between self-heating and ferroelectric properties in PZT ceramics during polarization reorientation, J. Phys. Condens. Matter 12 (2000) 5939.
[61] R. Ahluwalia, W. Cao, Influence of dipolar defects on switching behavior in ferroelectrics, Phys. Rev. B 63 (2001) 2103.
[62] D. Xu, W.L. Li, L.D. Wang, W. Wang, W.P. Cao, W.D. Fei, Large piezoelectric properties induced by doping ionic pairs in $BaTiO_3$ ceramics, Acta Mater. 79 (2014) 84–92.
[63] R.D. Shannon, Revised ionic radii and systematic studies of interatomic distances in halides and chalcogenides, Acta Crystallogr. A32 (1976) 751–767.
[64] Q. Lou, X. Shi, X. Ruan, J. Zeng, Z. Man, L. Zheng, G. Li, Ferroelectric properties of Li-doped $BaTiO_3$ ceramics, J. Am. Ceram. Soc. 101 (8) (2018) 3597–3604.
[65] Thorsten Leist, Torsten Granzow, Wook Jo, Jürgen Rödel, Effect of tetragonal distortion on ferroelectric domain switching: a case study on La-doped $BiFeO_3$–$PbTiO_3$ ceramics, J. Appl. Phys. 108 (2010), 014103.
[66] G. Schileo, L. Luisman, A. Feteira, M. Deluca, K. Reichmann, Structure–property relationships in $BaTiO_3$-$BiFeO_3$–$BiYbO_3$ ceramics, J. Eur. Ceram. Soc. 33 (2013) 1457–1468.
[67] F. Maxim, P. Ferreira, P.M. Vilarinho, I. Reaney, Hydrothermal synthesis and crystal growth studies of $BaTiO_3$ using Ti nanotube precursors, Cryst. Growth Des. 8 (9) (2008) 3309–3315.
[68] Y. Shiratori, C. Pithan, J. Dornseiffer, R. Waser, Raman scattering studies on nanocrystalline $BaTiO_3$ Part I-isolated particles and aggregates, J. Raman Spectrosc. 38 (2007) 1288–1299.
[69] Y. Shiratori, C. Pithan, J. Dornseiffer, R. Waser, Raman scattering studies on nanocrystalline $BaTiO_3$ Part II-consolidated polycrystalline ceramics, J. Raman Spectrosc. 38 (2007) 1300–1306.
[70] M.S. Alkathy, M.H. Lente, J.A. Eiras, Bandgap narrowing of $Ba_{0.92}Na_{0.04}Bi_{0.04}TiO_3$ ferroelectric ceramics by transition metals doping for photovoltaic applications, Mater. Chem. Phys. 257 (2021), 123791.
[71] V. Pal, O.P. Thakur, R.K. Dwivedi, Investigation of MPB region in lead free BLNT-BCT system through XRD and Raman spectroscopy, J. Phys. D Appl. Phys. 48 (2015), 05530.
[72] J. Kreisel, A. Glazer, M.G. Jones, P.A. Thomas, L. Abello, G. Lucazeau, An x-ray diffraction and Raman spectroscopy investigation of A-site substituted perovskite compounds: the $(Na_{1-x}K_x)0.5Bi_{0.5}TiO_3$ ($0 \leq x \leq 1$) solid solution, J. Phys. Condens. Matter 12 (2000) 3267–3280.
[73] J. Petzelt, S. Kamba, J. Fábry, D. Noujni, V. Porokhonskyy, A. Pashkin, G. E. Kugel, Infrared, Raman and high-frequency dielectric spectroscopy and the phase transitions in $Na_{1/2}Bi_{1/2}TiO_3$, J. Phys. Condens. Matter 16 (15) (2004) 2719–2731.
[74] J. Kreisel, A.M. Glazer, Pierre Bouvier, G. Lucazeau, High-pressure Raman study of a relaxor ferroelectric: the $Na_{0.5}Bi_{0.5}TiO_3$ perovskite, Phys. Rev. B 63 (17) (2001), 174106.
[75] V. Buscaglia, S. Tripathi, V. etkov, M. apiaggi, M. eluca, A. Gajović, Y. Ren, Average and local atomic-scale structure in $Ba(Zr_xTi_{1-x})O_3$ (x= 0.10, 0.20, 0.40) ceramics by high-energy X-ray diffraction and Raman spectroscopy, J. Condens. Matter Phys. 26 (2014), 065901.
[76] R. Kumar, K. Asokan, S. Patnaik, B. Birajdar, Evolution of microstructure and relaxor ferroelectric properties in $(La_zBa_{1-z})(Ti_{0.80}Sn_{0.20})O_3$, J. Alloys Compd. 687 (2016) 197–203.
[77] A. Kumar, I. Rivera, R. Katiyar, Investigation of local structure of lead-free relaxor Ba(Ti0.70Sn0.30)O3 by Raman spectroscopy, J. Raman Spectrosc. 40 (2009) 459–462.
[78] O. Cojocaru-Mirédin, J. Schmieg, M. Müller, A. Weber, E. Ivers-Tiffée, D. Gerthsen, Quantifying lithium enrichment at grain boundaries in $Li_7La_3Zr_2O_{12}$ solid electrolyte by correlative microscopy, J. Power Sources 539 (2022), 231417.
[79] Z. Yang, F. Gao, H. Du, L. Jin, L. Yan, Q. Hu, Y. Yu, S. Qu, X. Wei, Z. Xu, Y.-J. Wang, Grain size engineered lead-free ceramics with both large energy storage density and ultrahigh mechanical properties, Nano Energy 58 (2019) 768–777.
[80] P. Zhao, Z. Cai, L. Wu, C. Zhu, L. Li, X. Wang, Perspectives and challenges for lead-free energy-storage multilayer ceramic capacitors, J. Adv. Ceram. 10 (6) (2021) 1153–1193.
[81] M.A.M. Khan, S. Kumar, M. Ahamed, J. Ahmed, A. Kumar, M.A. Shar, J. Mater. Sci. Mater. Electron. 32 (2021) 12911–12921.
[82] M.H. Tang, J. Zhang, X.L. Xu, H. Funakubo, Y. Sugiyama, H. Ishiwara, J. Li, Electrical properties and x-ray photoelectron spectroscopy studies of $Bi(Zn_{0.5}Ti_{0.5})O_3$ doped $Pb(Zr_{0.4}Ti_{0.6})O_3$ thin films, J. Appl. Phys. 108 (8) (2010), 084101.
[83] Agda Eunice Souza, Silvio Rainho Teixeira, Cassio Morilla-Santos, Wido Herwig Schreiner, Paulo Noronha Lisboa Filho, Elson Longo, Photoluminescence activity of $Ba_{1-x}Ca_xTiO_3$: dependence on particle size and morphology, J. Mater. Chem. C 2 (34) (2014) 7056–7070.
[84] Bedri Erdem, Robert A. Hunsicker, Gary W. Simmons, E. David Sudol, Victoria L. Dimonie, Mohamed S. El-Aasser, XPS and FTIR surface characterization of TiO_2 particles used in polymer encapsulation, Langmuir 17 (9) (2001) 2664–2669.
[85] J. Liu, J.R. Xu, B. Cui, Q. Yu, S.J. Zhong, S.M. Du, D. Xu, Colossal permittivity characteristics and mechanism of (Sr, Ta) co-doped TiO_2 ceramics, J. Mater. Sci. Mater. Electron. 31 (2020) 5205–5213.
[86] X. Ren, Large electric-field-induced strain in ferroelectric crystals by point-defect-mediated reversible domain switching, Nat. Mater. 3 (2004) 91–94.
[87] M.A. Dar, K. Majid, K.M. Batoo, R.K. Kotnala, Dielectric and impedance study of polycrystalline $Li_{0.35-0.5}XCd0.\ 3N_{ix}Fe_{2.35-0.5x}O_4$ ferrites synthesized via a citrate-gel auto combustion method, J. Alloys Compd. 632 (2015) 307–320.
[88] P. Sateesh, J. Omprakash, G.S. Kumar, G. Prasad, Studies of phase transition and impedance behavior of $Ba(Zr,Ti)O_3$ ceramics, J. Adv. Dielectr. 5 (2015), 1550002, 01.
[89] H. Wang, P. Zhao, L. Chen, L. Li, X. Wang, Energy storage properties of $0.87BaTiO_3$-$0.13Bi(Zn_{2/3}(Nb_{0.85}Ta_{0.15})_{1/3})O_3$ multilayer ceramic capacitors with thin dielectric layers, J Adv. Ceram. 9 (2020) 292–302.
[90] B. Jiang, L.A. Bursill, Phenomenological theory of size effects in ultrafine ferroelectric particles of lead titanate, Phys. Rev. Lett. B. 60 (14) (1999) 9978.
[91] Hao-Cheng Thong, Li Zhao, Jing-Tong Lu, Chen-Bo-Wen Li, Yi-Xuan Liu, Qiannan Sun, Zhengqian Fu, Wei Yan, Ke Wang, Domain engineering in bulk ferroelectric ceramics via mesoscopic chemical inhomogeneity, Adv. Sci. 9 (17) (2022), 2200998.
[92] A. Li, Y. Wang, L. Yang, P. Yang, G. Wang, J. Chen, R. Wang, Ferroelectric relaxor behavior and dielectric properties of La/Y co-doped $(Ba_{0.9}Ca_{0.1})(Zr_{0.2}Ti_{0.8})O_3$ ceramics, J. Mater. Sci. Mater. Electron. 27 (2016) 6150–6155.
[93] L.E. Cross, Relaxor ferroelectrics: an overview, Ferroelectrics 151 (1) (1994) 305–320.
[94] X.G. Tang, J. Wang, X.X. Wang, H.L.W. Chan, Effects of grain size on the dielectric properties and turnabilities of sol–gel derived $Ba(Zr_{0.2}Ti_{0.8})O_3$ ceramics, Solid State Commun. 131 (3) (2004) 163–168.
[95] I.P. Studenyak, V.Y. Izai, A.I. Pogodin, O.P. Kokhan, V.I. Sidey, M.Y. Sabov, A. Kežionis, T. Šalkus, J. Banys, Structural and electrical properties of argyrodite-type Cu_7PS_6 crystals Lith, J. Phys. 57 (2017) 243–251.
[96] Z. Lu, G.e. Wang, W. Bao, J. Li, L. Li, A. Mostaed, H. Yang, H. Ji, D. Li, A. Feteira, F. Xu, D.C. Sinclair, D. Wang, S.-Y. Liu, I. M, Reaney Superior energy density through tailored dopant strategies in multilayer ceramic capacitors, Energy Environ. Sci. 13 (9) (2020) 2938–2948.
[97] H. Yang, F. Yan, Y. Lin, T. Wang, Enhanced energy storage properties of $Ba_{0.4}Sr_{0.6}TiO_3$ lead-free ceramics with Bi_2O_3-B_2O_3.SiO_2 glass addition, J. Eur. Ceram. Soc. 38 (4) (2018) 1367–1373.
[98] Wen-Bo Li, Di Zhou, Li-Xia Pang, Enhanced energy storage density by inducing defect dipoles in lead free relaxor ferroelectric $BaTiO_3$-based ceramics, Appl. Phys. Lett. 110 (13) (2017), 132902.
[99] Gui-wei Yan, Ming-gang Ma, Li Cheng-bo, Zhi-wei Li, Xiao-yu Zhong, Jian Yang, Fei Wu, Zhi-hui Chen, Enhanced energy storage property and dielectric breakdown strength in Li^+ doped $BaTiO_3$ ceramics, J. Alloys Compd. 857 (2021), 158021.
[100] S. Saremi, J. Kim, A. Ghosh, D. Meyers, L.W. Martin, Defect-induced (dis)order in relaxor ferroelectric thin films, Phys. Rev. Lett. 123 (2019), 207602.
[101] U. Robels, G. Arlt, Domain wall clamping in ferroelectrics by orientation of defects, J. Appl. Phys. 73 (7) (1993) 3454–3460.
[102] Z. Li, H.C. Thong, Y.F. Zhang, Z. Xu, Z. Zhou, Y.X. Liu, Y.Y.S. Cheng, S.H. Wang, C.L. Zhao, F. Chen, K. Bi, B. Han, K. Wang, Defect engineering in lead zirconate titanate ferroelectric ceramic for enhanced electromechanical transducer efficiency, Adv. Funct. Mater. 31 (1) (2021), 2005012.
[103] Lixin He, David Vanderbilt, First-principles study of oxygen-vacancy pinning of domain walls in $PbTiO_3$, Phys. Rev. B 68 (13) (2003), 134103.
[104] Tadej Rojac, Marija Kosec, Bojan Budic, Setter Nava, Dragan Damjanovic, Strong ferroelectric domain-wall pinning in $BiFeO_3$ ceramics, J. Appl. Phys. 108 (7) (2010), 074107.
[105] M.I. Morozov, D. Damjanovic, Charge migration in $Pb(Zr,Ti)O_3$ ceramics and its relation to ageing, hardening, and softening, J. Appl. Phys. 107 (3) (2010), 034106.
[106] Chen-Bo-Wen Li, Hao-Cheng Thong, Yi-Xuan Liu, Bi Ke, Zhengqian Fu, Ke Wang, Thermally induced domain reconfiguration in ferroelectric alkaline niobate, Adv. Funct. Mater. 32 (2022), 2204421.
[107] Zhi-Hao Zhao, Yejing Dai, Feng Huang, The formation and effect of defect dipoles in lead-free piezoelectric ceramics, a review, Sustain. Mater. Technol. 20 (2019), e00092.
[108] M.H. Lente, J.A. Eiras, 90° domain reorientation and domain wall rearrangement in lead zirconate titanate ceramics characterized by transient current and hysteresis loop measurements, J. Appl. Phys. 89 (2001) 5093.
[109] M.H. Lente, J.A. Eiras, Domain reorientation anisotropy in ferroelectric polycrystals, J. Appl. Phys. 92 (4) (2002) 2112–2117.